Biochemistry

Article

pubs.acs.org/biochemistry

Small Molecules Engage Hot Spots through Cooperative Binding To Inhibit a Tight Protein−Protein Interaction

Degang Liu,[†] David Xu,[§,∥] Min Liu,[§] William Eric Knabe,[†] Cai Yuan,[§] Donghui Zhou,[†] Mingdong Huang,[§] and Samy O. Meroueh*[,†,‡]

[†]Department of Biochemistry and [‡]Department of Molecular Biology, Center for Computational Biology and Bioinformatics, Indiana University School of Medicine, Indianapolis, Indiana 46202, United States

[§]Fujian Institute of Research on the Structure of Matter, Chinese Academy of Science, Gulou District, Fuzhou, Fujian 350002, China

[∥]Department of BioHealth Informatics, Indiana University School of Informatics and Computing, Indianapolis, Indiana 46202, United States

Supporting Information

ABSTRACT: Protein−protein interactions drive every aspect of cell signaling, yet only a few small-molecule inhibitors of these interactions exist. Despite our ability to identify critical residues known as hot spots, little is known about how to effectively engage them to disrupt protein−protein interactions. Here, we take advantage of the ease of preparation and stability of pyrrolinone **1**, a small-molecule inhibitor of the tight interaction between the urokinase receptor (uPAR) and its binding partner, the urokinase-type plasminogen activator uPA, to synthesize more than 40 derivatives and explore their effect on the protein−protein interaction. We report the crystal structure of uPAR bound to previously discovered pyrazole **3** and to pyrrolinone **12**. While both **3** and **12** bind to uPAR and compete with a fluorescently labeled peptide probe, only **12** and its derivatives inhibit the full uPAR·uPA interaction. Compounds **3** and **12** mimic and engage different hot-spot residues on uPA and uPAR, respectively. Interestingly, **12** is involved in a π−cation interaction with Arg-53, which is not considered a hot spot. Explicit-solvent molecular dynamics simulations reveal that **3** and **12** exhibit dramatically different correlations of motion with residues on uPAR. Free energy calculations for the wild-type and mutant uPAR bound to uPA or **12** show that Arg-53 interacts with uPA or with **12** in a highly cooperative manner, thereby altering the contributions of hot spots to uPAR binding. The direct engagement of peripheral residues not considered hot spots through π−cation or salt-bridge interactions could provide new opportunities for enhanced small-molecule engagement of hot spots to disrupt challenging protein−protein interactions.

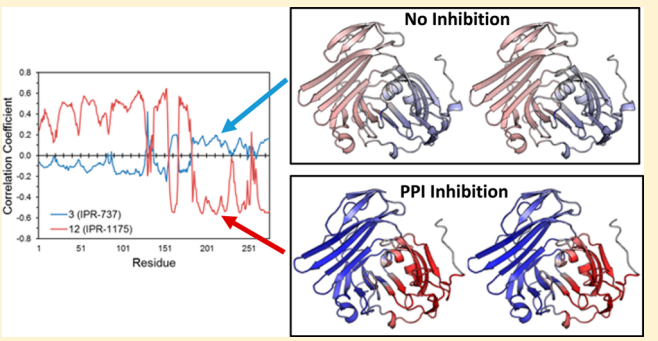

It is estimated that there are more than 200000 protein−protein interactions in a cell. These interactions drive nearly every aspect of cellular function. Small molecules offer an opportunity to explore these interactions in normal and pathological processes. Protein−protein interactions exhibit a wide range of binding thermodynamics and kinetics from weak interactions that occur over small interfaces to tight and stable protein−protein interactions that occur over large interfaces (>1000 Å^2). Although the design of small molecules to disrupt weak interactions is relatively straightforward, inhibiting tight interactions is much more challenging. To date, while numerous small molecules have been reported to inhibit protein−protein interactions (reviewed in refs 1 and 2), there are only a few examples of small molecules that disrupt tight protein−protein interactions (K_d = 1−100 nM); examples include antagonists of Bcl-xL[3] and IL-2R.[4] The ability to disrupt these tight interactions that occur over large surfaces with a small molecule that has a much smaller footprint is attributed to the presence of residues that contribute disproportionately to the binding affinity, also known as hot spots.[5−9]

The urokinase receptor (uPAR) is a cell surface glycosphosphatidylinositol (GPI)-anchored receptor that is part of an extensive network of protein−protein interactions. Its binding partners include serine proteinase urokinase-type plasminogen activator uPA[10] and the glycoprotein vitronectin.[11−13] The uPAR·uPA protein−protein interaction is a high-affinity (K_D = 1 nM) and stable (k_{off} = 10^{-4} s^{-1}) interaction.[14] Crystal structures of the uPAR·uPA complex show that uPA binds to uPAR along a well-defined binding site that is part of a >1000 Å^2 interface.[15−18] The interaction is mediated by a 25-residue growth factor-like domain (GFD), and residues from a kringle-like domain of uPA. A comprehensive alanine scanning study at

Received: October 10, 2016
Revised: February 2, 2017
Published: February 10, 2017

DOI: 10.1021/acs.biochem.6b01039
Biochemistry XXXX, XXX, XXX−XXX

the uPAR·uPA interface identified several hot-spot residues that reduced the uPAR·uPA binding affinity by >1 kcal mol^{-1}.[14,18,19] In the uPAR·uPA complex, there are hot spots both on uPA (Trp-30, Phe-25, Tyr-24, and Ile-28)[14] and on the large binding cleft of uPAR that accommodates the GFD domain (Leu-150, Leu-55, Leu-66, Tyr-57, and Asp-140).[18]

Previously, we performed a computational screen of commercial libraries to identify small molecules that bind to uPAR and disrupt the uPAR·uPA protein−protein interaction.[18,21,22] Compound **1** was discovered following a substructure search using pyrazole, piperidinone, and pyrrolydinone compounds as templates.[23] These compounds were shown to bind to uPAR and displace a fluorescently labeled peptide. In addition to **1**, another strategy that consisted of docking chemical libraries to an ensemble of uPAR structures sampled from explicit-solvent molecular dynamics simulations led to **2** (IPR-803).[24] Compound **2** binds to uPAR with submicromolar affinity and inhibits the uPAR·uPA complex with single-digit micromolar IC_{50} values.[24] Structure−activity relationships revealed the critical nature of a benzoic acid moiety that was attributed to a salt-bridge interaction with the guanidinium group of Arg-53. We showed that this residue became exposed following explicit-solvent molecular dynamics simulations.[16] Our predicted binding mode and interaction with Arg-53 was recently independently confirmed by a crystal structure of an analogue of **2** bound to uPAR.[25] To the best of our knowledge, our work with **2** is the first study that led to small-molecule protein−protein antagonists using protein structures sampled from molecular dynamics simulations. The work highlights the importance of considering molecular dynamics of a receptor for the design of small molecules that disrupt tight interactions (Scheme 1).

Scheme 1

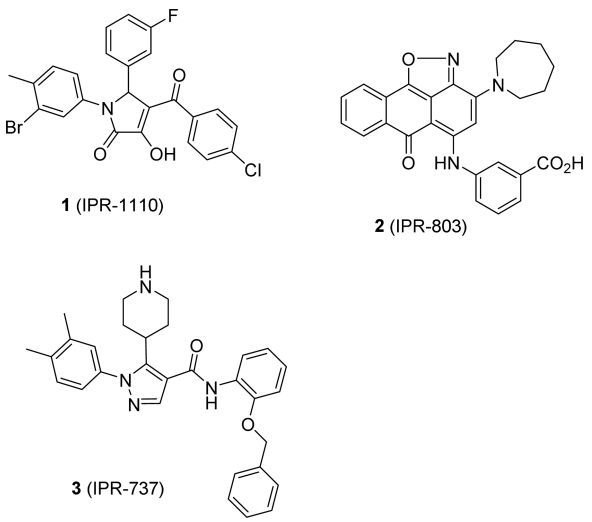

Analysis of three-dimensional structures of protein−protein complexes reveals that hot spots are generally found at the protein−protein interface of tight protein−protein interactions.[5,26,27] They can be located either on the ligand or on the receptor that harbors a binding site. It has been suggested that small molecules that bind to hot spots can disrupt tight protein−protein interactions despite their smaller footprint. Early work targeting the IL-2·IL-2Rα complex confirmed that small molecules that inhibited the interaction directly bind to hot spots,[28] but the researchers also found that neighboring residues that promote IL-2·IL-2Rα enhanced binding of small molecules. These counterintuitive results can be explained by dynamical effects likely arising from the cooperativity of residues at the interface.[29] This cooperativity has led to the suggestion that hot-spot clusters can form hot regions.[30] Cooperativity makes it more difficult to select the appropriate hot spots for the rational design of small-molecule inhibitors of protein−protein interactions. The mere binding to hot spots may not necessarily result in more potent inhibition of the protein−protein interaction. A deeper understanding of (i) the interaction energies between small molecules and individual residues and (ii) the dynamical changes that occur upon binding of a small molecule could lead to more effective strategies for the rational design of small-molecule protein−protein interaction inhibitors.

Here, we take advantage of the straightforward synthesis of **1** to prepare 46 derivatives of the compound to gain insight into the forces that lead to small-molecule inhibition of the uPAR·uPA protein−protein interaction. Their activity was measured using fluorescence polarization with a labeled α-helical peptide and an enzyme-linked immunosorbent assay (ELISA) that uses uPA_{ATF}, which includes the entire binding interface of the uPAR·uPA interface. We determine the crystal structure of uPAR bound to two small molecules, namely, pyrrolinone **21** (IPR-1175) and pyrrazole **3** (IPR-737), providing a structural basis for the activity of **1** and its derivatives. To gain deeper insight into the basis for the activity of **1** and its derivatives, we conducted explicit-solvent molecular dynamics simulations of uPAR in complex with uPA, **1**, **3**, and several other derivatives. The resulting structures were used for free energy calculations using molecular mechanics (MM), generalized Born (GB), and solvent-accessible surface (SA) also known as MM-GBSA. Decomposition energy calculations, which correspond to the MM-GBSA free energy between a ligand and individual residues on uPAR, provided deeper insight into the individual contributions of each amino acid to the protein−protein and protein−compound interactions. Finally, we compare the dynamics of the uPAR·uPA interaction with the dynamics of uPAR in complex with small molecules.

MATERIALS AND METHODS

Protein Expression and Purification. suPAR was obtained by a one-step purification process as previously described.[31]

Crystallization and Structure Determination of uPAR in Complex with Its Inhibitor, 3 (IPR-737), and 12 (IPR-1175). A stabilized form of human soluble uPAR (H47C/N259C) (denoted suPARcc) was used to facilitate crystallization of suPAR in complex with the inhibitor. suPARcc was expressed and purified as previously described[32] and concentrated to 16 mg mL^{-1}. Crystals were formed using 1.96 M ammonium sulfate, 100 mM HEPES (pH 7.5), and 2% (w/v) polyethylene glycol 400 as the precipitant solution by the sitting-drop vapor diffusion method. Crystals were soaked into 40% PEG4000 and 100 mM HEPES (pH 7.5) with 1 mM **3** (IPR-737) or **12** (IPR-1175) for ∼2 days. X-ray diffraction data was collected under cryogenic conditions at 100 K. Crystals were collected on beamline BL17U at the Shanghai Synchrotron Radiation Facility (SSRF) and were processed, integrated, and scaled together with HKL2000.[33] The crystal structures of the suPARcc·**3** (IPR-737) complex and suPARcc·**12** (IPR-1175) complex were determined by the molecular

DOI: 10.1021/acs.biochem.6b01039
Biochemistry XXXX, XXX, XXX−XXX

Table 1. Synthesized Derivatives

Compounds	R_1	R_2	R_3	IC_{50}(μM)	K_i (μM)	MW[a]	AlogP	HBA[b]	HBD[c]	RB[d]
1 (IPR1110)			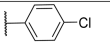	18.4	0.7	499.7	5.4	2	0	4
4 (IPR1201)			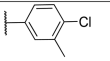	16.3±1.9	1.0±0.2	513.8	5.8	2	0	4
5 (IPR1200)			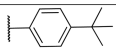	27.4±2.1	2.7±0.4	521.4	6.1	2	0	5
6 (IPR1181)				30.2±2.0	3.8±0.4	465.3	4.7	2	0	4
7 (IPR1178)			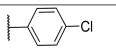	20.2±1.9	1.1±0.2	516.2	5.8	2	0	4
8 (IPR1187)		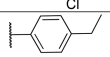	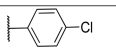	26.4±1.6	2.5±0.5	509.8	6.1	2	0	5
9 (IPR1185)		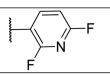	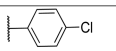	35.6±5.6	1.7±0.1	518.7	5.2	3	0	4
10 (IPR1192)			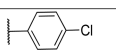	30.1±2.6	1.9±0.4	499.7	5.4	2	0	4
11 (IPR1193)		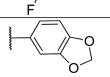	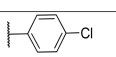	57.8±1.9	1.7±0.1	525.8	4.9	4	0	4
12 (IPR1175)			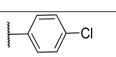	45.2±2.1	2.0±0.5	448.9	5.3	2	0	5
13 (IPR1171)			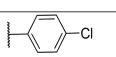	23.0±2.3	1.3±0.1	546.7	5.2	2	0	4
14 (IPR1194)			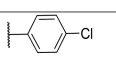	66.7±7.2	4.5±0.9	448.9	5.3	2	0	5
15 (IPR1195)			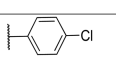	61.7±5.1	1.6±0.3	462.9	5.5	2	0	5
16 (IPR1186)	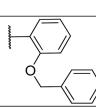		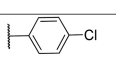	35.3±2.0	2.1±0.4	512.9	5.7	3	0	7
17 (IPR1182)			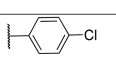	37.1±2.9	1.3±0.2	471.3	4.8	3	0	5
18 (IPR1196)			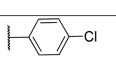	47.3±2.4	3.6±0.8	453.9	4.4	4	0	5
19 (IPR1152)			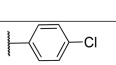	ND	95.2±1.6	450.9	3.8	3	1	6
20 (IPR1119)			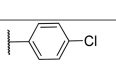	66.5±2.4	8.6±2.1	489.9	5.2	2	0	5
21 (IPR1183)		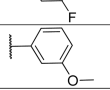		91.1±3.2	13.3±2.9	477.3	4.5	3	0	5
22 (IPR1176)			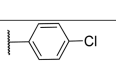	53.8±6.5	1.9±0.4	507.0	6.4	3	0	10
23 (IPR1174)			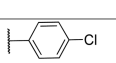	18.4±4.9	1.2±0.2	521.0	6.8	3	0	10
24 (IPR1179)		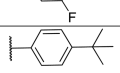	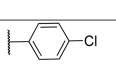	ND	15.9±2.8	537.9	6.6	2	0	5
25 (IPR1177)			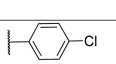	ND	ND	430.9	3.6	3	1	9
26 (IPR1188)			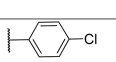	ND	2.0±0.6	452.9	4.7	2	0	6
27 (IPR1189)			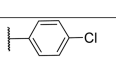	ND	11.8±1.8	499.7	5.4	2	0	4
28 (IPR1190)		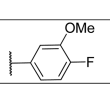	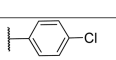	21.0±0.7	2.6±0.2	529.8	5.3	3	0	5
29 (IPR1191)			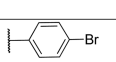	29.5±3.3	2.1±0.2	544.2	5.4	2	0	4

DOI: 10.1021/acs.biochem.6b01039
Biochemistry XXXX, XXX, XXX−XXX

Table 1. continued

Compounds	R_1	R_2	R_3	IC_{50}(μM)	K_i (μM)	MW[a]	AlogP	HBA[b]	HBD[c]	RB[d]
30 (IPR1150)	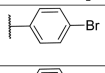		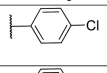	ND	ND	485.7	4.9	2	0	4
31 (IPR1151)	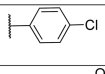		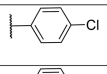	69.0±1.2	31.7±2.6	441.3	4.8	2	0	4
32 (IPR1153)			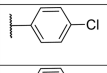	46.9±3.3	4.5±1.4	464.9	4.4	3	0	7
33 (IPR1157)	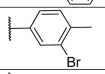		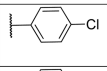	ND	17.6±1.6	495.8	5.6	2	0	4
34 (IPR1158)	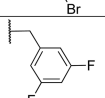		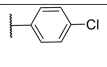	ND	2.3±0.3	456.8	4.5	2	0	5
35 (IPR1159)	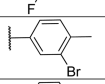		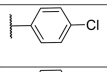	ND	ND	511.8	5.1	3	0	5
36 (IPR1160)	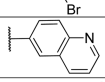		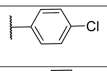	ND	1.9±0.3	456.9	5.0	2	0	4
37 (IPR1161)	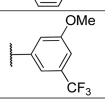		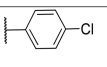	87.5±6.1	18.6±1.8	504.8	5.1	3	0	6
38 (IPR1167)	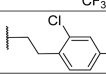		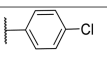	ND	2.3±0.2	503.8	5.8	2	0	6
39 (IPR1168)	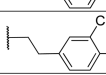		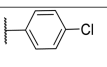	23.1±1.6	0.9±0.0	503.8	5.8	2	0	6
40 (IPR1172)	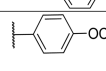		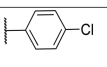	93.3±1.6	3.7±0.5	490.8	6.2	3	0	6
41 (IPR1173)	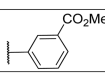		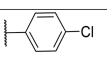	97.8±1.0	7.7±0.8	464.8	4.0	4	0	6
42 (IPR1197)	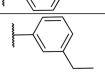		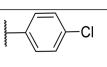	77.1±3.4	5.5±0.6	434.9	5.1	2	0	5
43 (IPR1198)	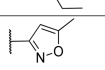		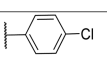	ND	55.3±2.0	411.8	2.9	4	0	4
44 (IPR1607)	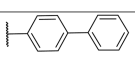		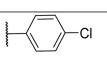	24.0±3.2	0.8±0.1	482.9	5.6	2	0	5
45 (IPR2260)	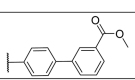		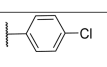	15.7±1.3	0.4±0.1	569.0	5.8	4	0	9
46 (IPR1609) XHS12	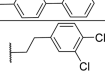		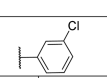	21.6±1.6	0.6±0.1	540.9	5.5	4	0	7

Compounds	R_1	R_2	R_3	R_4	IC_{50} (μM)	K_i (μM)	MW[a]	AlogP	HBA[b]	HBD[c]	RB[d]
47 (IPR1154)	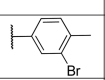		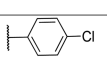	Me	ND	33.5±2.2	514.8	6.1	3	0	5
48 (IPR1155)	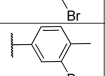		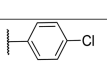	^{i}Pr	ND	ND	542.8	6.8	3	0	6

[a]Molecular weight. [b]Hydrogen bond acceptor. [c]Hydrogen bond donor. [d]Rotatable bonds.

replacement program MOLREP[34] of the CCP4 package using Protein Data Bank (PDB) entry 3U74 as a search model. After molecular replacement, inhibitor **3** (IPR-737) or **12** (IPR-1175) was built into the model on the basis of a $2F_{obs} - F_{calc}$ σ-weighted composite omit map, and then iterative manual model building and model refinement were performed with COOT[35] and REFMAC, yielding a final R value of 0.2119 and an R_{free} value of 0.2576 in the suPARcc·**3** (IPR-737) complex (Table S2), while the values were 0.2349 and 0.2613, respectively, in the suPARcc·**12** (IPR-1175) complex (Table S1). These structures were analyzed by PyMOL.[4]

Fluorescence Polarization. Polarized fluorescence intensities were measured using an EnVision Multilabel plate reader (PerkinElmer) with excitation and emission wavelengths of 485 and 530 nm, respectively.[24] A Thermo Scientific Nunc 384-well black microplate was used to prepare samples with a final volume of 50 μL in duplicate. First, the compounds were serially diluted in dimethyl sulfoxide (DMSO) and further diluted in 1× PBS buffer with 0.01% Triton X-100 to yield a final concentration from 100 to 0.046 μM. Triton X-100 was added in the buffer to avoid compound aggregation; 35 μL of the compound solution and 10 μL of PBS containing uPAR were added to the wells, and the mixture was incubated for at least 15 min to allow the compound to bind to the protein. Finally, 5 μL of fluorescent AE147-FAM peptide was added for a total volume of 50 μL in each well, resulting in final uPAR and peptide concentrations of 320 and 100 nM, respectively. The final DMSO concentration was 2%, which had no effect on the binding of the peptide. Controls included wells containing only the peptide and wells containing both protein and peptide each

DOI: 10.1021/acs.biochem.6b01039
Biochemistry XXXX, XXX, XXX−XXX

in quadruplicate to ensure the validity of the reaction assay. A unit of millipolarization (mP) was used to calculate the percent inhibition of the compounds. Inhibition constants were determined using the K_i calculator available at http://sw16.im.med.umich.edu/software/calc_ki/.

Microtiter-Based ELISA for uPAR·uPA. High-binding microplates (Greiner Bio-One) were incubated for 2 h at 4 °C with 100 μL of 2 μg mL^{-1} uPA_{ATF} in PBS. Each plate was washed with 0.05% Tween 20 in PBS buffer between each step. A 1:1 mixture of Superblock buffer in PBS (Thermo Fisher Scientific, Inc., Waltham, MA) with 0.04 M NaH_2PO_4 and 0.3 M NaCl buffer was used for blocking at room temperature for 1 h; 100 μL of 75 nM uPAR in PBS with 0.025% Triton X-100 was added with the indicated concentrations of compounds. Compounds were screened initially at 50 μM. For concentration-dependent studies, a range of compound concentrations from 100 to 0.4 μM were used. The final DMSO concentration was 1%. Following incubation for 30 min and subsequent washing steps, the human uPAR biotinylated antibody (1:3000 dilution of 0.2 mg mL^{-1} BAF807, R&D Systems, Minneapolis, MN) in PBS containing 1% BSA was added to the wells (100 μL/well) and incubated for 1 h to allow for the detection of bound uPAR. Following washing, 100 μL of streptavidin-bound horseradish peroxidase (84 ng mL^{-1}) in PBS containing 1% BSA was added for 20 min. The signal obtained in the presence of TMB in phosphate-citrate buffer (pH 5) and hydrogen peroxide was stopped by adding a H_2SO_4 solution and detected using a SpectraMax M5e instrument (Molecular Devices, Sunnyvale, CA).

Molecular Docking. Small molecules were prepared for molecular docking using Maestro (version 9.4, Schrödinger, LLC, New York, NY). Compounds were first processed with LigPrep (version 2.6, Schrödinger, LLC). The receptor protein structure (PDB entry 3BT1 and crystal structures of the uPAR·**3** and uPAR·**12** complexes) was prepared using the Protein Preparation Wizard workflow in Maestro. Bond orders were assigned, hydrogen atoms added, and disulfide bonds created. For the 3BT1 structure, vitronectin (chain B) was removed and the missing loop at residues Arg-83 and Ala-84 introduced using the Prime[36] module in Schrödinger. The missing loops from Ser-81 to Ser-90 (uPAR·**3**) and from Ile-129 to Lys-139 (uPAR·**3** and uPAR·**12**) were reconstructed using the *loop-model* class in MODELER (version 9.13).[37] Five initial models were constructed and refined using the "fast" molecular dynamics (MD) annealing function. Five additional loop models were constructed for each initial model and similarly refined. A loop model was visually selected from the 25 loop models that best matched the existing loop in the 3BT1 structure. Finally, structures were protonated at pH 7.0 using PROPKA.[38]

The binding poses of select derivatives of **1** (IPR-1110) were generated using the cocrystal structure of uPAR in complex with **3** (IPR-1175) as a guide in Maestro. The derivatives were docked in a 21 Å box centered on the complexed ligand using Glide[39] (Schrödinger, LLC) in standard precision (SP) mode. The common core structure of the analogues found in Table 1 was used to restrict the binding poses of the derivative compounds. All other parameters were set to default values.

Molecular Dynamics Simulations. The binding poses were used to run MD simulations using the AMBER14 and AmberTools15 packages.[40] Each compound was assigned AM1-BCC[41] charges and gaff[42] atom types using the *antechamber* program.[43] Complexes were immersed in a box of TIP3P[44] water molecules. No atom on the complex was within 14 Å of any side of the box. The solvated box was further neutralized with Na^+ or Cl^- counterions using the *tleap* program.

Simulations were performed using the GPU accelerated version of the *pmemd* program with ff12SB[45] and gaff[42] force fields under periodic boundary conditions. All bonds involving hydrogen atoms were constrained by using the SHAKE algorithm,[46] and a 2 fs time step was used in the simulation. The particle mesh Ewald[47] (PME) method was used to treat long-range electrostatics. Simulations were run at 298 K under 1 atm in the *NPT* ensemble employing a Langevin thermostat and a Berendsen barostat. Water molecules were first energy-minimized and equilibrated by running a short simulation with the complex fixed using Cartesian restraints. This was followed by a series of energy minimizations in which the Cartesian restraints were gradually relaxed from 500 to 0 kcal Å^{-2}, and the system was subsequently gradually heated to 298 K via a 48 ps MD run. Via assignment of different initial velocities, 10 independent simulations that are 10 ns in length each were performed for the protein−compound structures.

Free Energy Calculations. In each of the 10 trajectories (10 ns in length), the first 2 ns was discarded for equilibration. MD snapshots were saved every 1 ps, yielding 8000 structures per trajectory. A total of 80000 snapshots were generated per 100 ns of simulation; 1000 snapshots were selected at regular intervals from the 80000 snapshots for free energy calculations using the *cpptraj* program.[48] The molecular mechanics-generalized Born surface area (MM-GBSA)[49] method was used to calculate the free energy using the *MMPBSA.py* script[50] and Onufriev's GB model.[51,52] Solvent-accessible surface area (SASA) calculations were switched to the ICOSA method, where surface areas are computed by recursively approximating a sphere around an atom, starting from an icosahedron. Salt concentrations were set to 0.1 M. The entropy was determined by normal mode calculations[53] with the *nmode* module from 100 of the 1000 snapshots used in the free energy calculations. The maximal number of cycles of minimization was set to 10000. The convergence criterion for the energy gradient to stop minimization was 0.5.

The MM-GBSA binding free energy is expressed as

$$\Delta G_{\text{MM-GBSA}} = \Delta E_{\text{GBTOT}} - T\Delta S_{\text{NM}}$$

where ΔE_{GBTOT} is the combined internal and solvation energies, T is the temperature, and ΔS_{NM} is the entropy determined by normal mode calculation. The solvation energy is determined using generalized Born (GB) solvation models (ΔE_{GBSOL}) (igb = 2):

$$\Delta E_{\text{GBTOT}} = \Delta E_{\text{GBSOLV}} + \Delta E_{\text{GAS}}$$

where ΔE_{GBSOLV} is the solvation free energy and ΔE_{GAS} is the molecular mechanical energies (gas phase). The gas-phase energies are composed of two components:

$$\Delta E_{\text{GAS}} = \Delta E_{\text{ELE}} + \Delta E_{\text{VDW}}$$

where ΔE_{ELE} is the nonpolar electrostatic energy and ΔE_{VDW} is the polar van der Waals energy. The GB solvation free energy is expressed by

$$\Delta E_{\text{GBSOLV}} = \Delta E_{\text{SURF}} + \Delta E_{\text{GB}}$$

where ΔE_{SURF} and ΔE_{GB} are the nonpolar and polar contributions to the solvation free energy, respectively. All the binding energies are determined by

DOI: 10.1021/acs.biochem.6b01039
Biochemistry XXXX, XXX, XXX−XXX

$$\Delta E = E^{COM} - E^{REC} - E^{LIG}$$

where E^{COM}, E^{REC}, and E^{LIG} are total energies corresponding to the complex, receptor, and ligand, respectively.

Decomposition Energy. The decomposition energy used in this work was determined using the *MMPBSA.py* script[50] available in AMBER14. The script provides several schemes for decomposing calculated free energies into specific residue contributions using either GB or PB implicit-solvent models. These schemes were developed by Gohlke and co-workers.[54] The per-residue decomposition scheme was used in this work. Similar to the free energy calculations, we use the GB solvation model from Onufriev and co-workers.[51,52] The energy terms are decomposed according to the scheme outlined in the AMBER14 manual using the following equation:

$$\begin{aligned}\Delta E_{decomp} = &\sum_{j\in COMPLEX \wedge j\in RECEPTOR} [\langle E^{COMPLEX}(i,j)\rangle \\ &- \langle E^{RECEPTOR}(i,j)\rangle] \\ &+ \sum_{j\in COMPLEX \wedge j\in LIGAND} [\langle E^{COMPLEX}(i,j)\rangle \\ &- \langle E^{LIGAND}(i,j)\rangle]\end{aligned}$$

where the first and second terms represent the average contribution over snapshots i from the MD simulation in residues j on the receptor and ligand, respectively. The term $E(i,j)$ corresponds to the contribution of the gas-phase and solvation energies, that is

$$\begin{aligned}E(i,j) &= E_{GAS}(i,j) + E_{GBSOLV}(i,j) \\ &= E_{VDW}(i,j) + E_{ELE}(i,j) + E_{GB}(i,j) + E_{SURF}(i,j)\end{aligned}$$

where E_{VDW} and E_{ELE} are the van der Waals and electrostatic energies in the gas phase (E_{GAS}), respectively. E_{GB} and E_{SURF} are the polar and nonpolar contributions to the solvation free energy by the GB solvation model (E_{GBSOLV}), respectively. Entropy is not included in the decomposition method.

The GB model is described in detail by Onufriev and associates[55] and in the AMBER14 manual. The GB model we selected (igb = 2, GB^{OBC} model I) approximates the solvation electrostatic E_{GB} by an analytical formula:

$$E_{GB} = -\frac{1}{2}\sum_{ij}\frac{q_i q_j}{f^{GB}}\left[1 - \frac{\exp(-Kf^{GB})}{\varepsilon}\right]$$

where r_{ij} is the distance between atoms i and j, R_i and R_j are the effective Born radii of atoms i and j, respectively, K is the Debye–Hückel screening parameter, ε is the dielectric constant, and f^{GB} is a smooth function. Each atom in the GB model is represented as a sphere with radius ρ_i with charge q_i. The f^{GB} function is expressed as

$$f^{GB} = \sqrt{r_{ij}^2 + R_i R_j \exp\left(-\frac{r_{ij}^2}{4R_i R_j}\right)}$$

and is used to describe the distance between two atoms and their effective Born radii.

The nonpolar contribution to the solvation free energy is calculated by approximating the total SASA of the molecule:

$$E_{SURF} = \gamma SASA + \beta$$

where γ and β are the surface tension and offset terms, respectively. The ICOSA method is used to determine SASA.[40,54] In this method, surface areas are computed by recursively approximating a sphere around an atom. The first sphere is modeled as an icosahedron. In each subsequent step, the faces of the polyhedron are divided into four equal-sized triangles to better approximate the sphere.

Chemistry. All chemicals were purchased from commercially available sources and used as received. Column chromatography was performed with silica gel (25–63 μm). High-resolution mass spectra were recorded on an Agilent 6520 Accurate Mass Q-TOF instrument. ^{1}H nuclear magnetic resonance was recorded in $CDCl_3$ or DMSO on a Bruker 500 MHz spectrometer. Reverse-phase liquid chromatography and mass spectrometry were performed on an Agilent 1100 LC/MSD instrument fitted with an Eclipse XBD-C18 (4.6 mm × 150 mm) column eluting at 1.0 mL min^{-1} employing an (acetonitrile/methanol)/water gradient (each containing 5 mM NH_4OAc) from 70 to 100% acetonitrile/methanol over 15 min and holding at 100% acetonitrile/methanol for 2 min. Chemical shifts are reported in parts per million using either residual $CHCl_3$ or DMSO as an internal reference. All compounds are >95% pure unless otherwise stated. Syntheses of 3-(hexyloxy)-aniline and 3-(hexyloxy)-4-methylaniline were performed using a protocol described by Marco and co-workers.[56] β-Diketoesters were synthesized with modification according to Milagre and co-workers.[57] Derivatives of **1** were synthesized by a modified procedure of Rose and co-workers.[58] Full compound characterization is provided in the Supporting Information.

RESULTS

Synthesis of Pyrrolinones, Stability, Reactivity, and Selectivity Studies. The ease of synthesis of **1** (IPR-1110) prompted us to prepare 46 derivatives to explore the uPAR·uPA binding interface (Table 1). **1** (IPR-1110) was modified at three sites, R_1–R_3. Most of the structure–activity exploration was focused on R_1 and R_2. The synthesis of these compounds was straightforward (Figure S1) as described previously.[23]

The pyrrolinone core structure of **1** suggests that nucleophilic residues within a protein could potentially form covalent adducts through nucleophilic attack at the carbon bearing the hydroxyl group of the core five-membered ring. To explore this possibility, we employed electrospray ionization (ESI) mass spectrometry. As shown in Figure S2, there was no adduct formation when uPAR was incubated with the compound, ruling out nonspecific covalent bond formation as the mechanism by which the pyrrolinone compounds antagonize uPAR–protein interactions. Next, we investigated the stability of the compound in buffer (PBS), methanol, and uPAR using high-performance liquid chromatography (Figure S3). The UV spectra for all three conditions were identical (Figure S3a), and the mass spectra corresponding to the major peaks were also identical (Figure S3b). This suggests that the compound is stable both in buffer and in the presence of uPAR.

Finally, we investigated the selectivity of the pyrrolinone compounds by testing them for inhibition of an unrelated protein–protein interaction between the α and β subunits of the CaV2.2 calcium channel (Figure S4). The CaV$\alpha\beta$ interaction is mediated by a tight single-digit nanomolar interaction that occurs over a large interface consisting primarily of an α helix of the α subunit binding to a large well-defined pocket on the β subunit (Figure S4). Compound **1**

DOI: 10.1021/acs.biochem.6b01039
Biochemistry XXXX, XXX, XXX–XXX

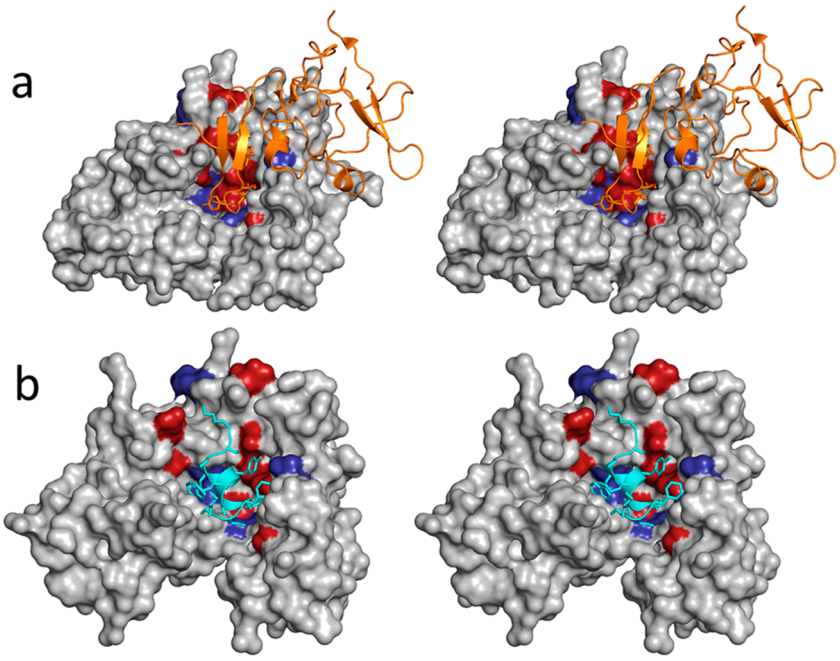

Figure 1. (a) Three-dimensional structure of the uPAR·uPA$_{ATF}$ complex (PDB entry 2FD6). uPAR is shown as a gray solvent-accessible surface. Residues whose mutations to alanine result in changes in binding affinity of ≥1 kcal mol^{-1} are colored red, while those that lead to changes between 0.5 and 1 kcal mol^{-1} are colored purple. uPA$_{ATF}$ is shown as an orange cartoon. (b) Three-dimensional structure of uPAR in complex with the AE-157 peptide (PDB entry 1YWH). The peptide is shown as a cyan cartoon, and side chains that come in contact with uPAR are shown as capped sticks. uPAR is rendered and color-coded in a manner similar to that of panel a.

(Figure S4) showed no inhibition of this interaction up to 25 μM. The effect of **1** on the CaV$\alpha\beta$ interaction at 50 and 100 μM can be attributed to aggregation considering the sharp rise in activity from nearly 0% inhibition at 25 μM to more than 75% inhibition at 50 μM. This was not observed for uPAR, whereby **1** exhibited a gradual increase in its level of inhibition of binding of AE-147 to uPAR (Figure S4). These studies confirm that the compounds bind to uPAR in a selective manner as evidenced by the lack of activity against another unrelated protein−protein interaction. It is possible that compound **1** inhibits interactions that are similar to the uPAR·uPA interaction. Future studies that explore compounds in cell culture should explore these compounds for inhibition of interactions that are similar to uPAR·uPA interactions.

Crystal Structures of Compounds Bound to uPAR. The crystal structure of uPAR was previously determined in complex with ATF (PDB entry 2FD6) (Figure 1a) or α-helical peptide AE-147 (PDB entry 1YWH) (Figure 1b). These structures revealed a large interface between uPAR and uPA that contains several hot spots, including Leu-55, Tyr-57, Leu-66, Asp-140, and Leu-150. All the hot spots on uPAR at the uPAR·uPA interaction are listed in Table S1. We hypothesized that compounds that disrupt the protein−protein interaction between uPAR and uPA likely directly engage these hot spots. To test this hypothesis, we resorted to X-ray crystallography to determine the structure of **1** (IPR-1110) and derivatives in complex with uPAR. We also attempted to determine the structures of pyrazole, piperidinone, pyrrolidinone, and butanamine compounds that we had previously shown to bind to uPAR.[21] We obtained structures for two compounds bound to uPAR, namely, pyrrolinone **12** (IPR-1175) (Figure 2 and Table S2) and pyrazole **3** (IPR-737) (Figure 3 and Table S3).

The structure of uPAR in complex with **12** reveals that the compound is ensconced deeply in the pocket that is occupied by the growth factor-like domain of uPA in its complex with uPAR (Figure 2a). The R$_1$ isopropylphenyl group of the compound points toward the interior of the hydrophobic pocket of uPAR. This pocket accommodates the residues located on the loop of the β turn of the GFD domain of uPA. The substituent makes direct contacts with Leu-150, Leu-168, Val-125, Leu-55, and Arg-53 (Figure 2b). Most of these interactions are hydrophobic except for the cation−π interaction with Arg-53. Cation−π interactions are commonly observed in protein−compound structures and can contribute up to 1 kcal mol^{-1} to the free energy of binding.[59,60] Here, the benzene ring of the R$_1$ group of **12** (IPR-1175) directly faces one of the Nω atoms of the guanidinium ion of Arg-53. The Nω atom is 2.5 Å from one of the *ortho* carbon atoms of the benzene ring. Unlike R$_1$, the chlorobenzene R$_3$ group of **12** (IPR-1175) points in the opposite direction and occupies a pocket surrounded by residues Thr-27, Val-29, Arg-142, and Leu-40 on uPAR. The R$_3$ group is more exposed to solvent than R$_1$ and does not occupy a pocket composed entirely of hydrophobic residues as evidenced by the presence of Arg-142. Finally, the R$_2$ group of **12** does not occupy a well-defined pocket on uPAR, but it is worth noting that this group is also involved in a cation−π interaction with Arg-53 of uPAR (Figure 2b). Interestingly, the R$_1$ and R$_3$ groups of **12** occupy the same position as uPA hot spots Ile-28 and Tyr-24, respectively (Figure 2c).

3 (IPR-737) adopts a binding mode different from that of **12** (IPR-1175) (Figure 3). **3** (IPR-737) binds outside the hydrophobic pocket of uPAR that is occupied by side chains of the β-turn loop of the GFD domain of uPA (Figure 3a). Unlike **12** (IPR-1175), the compound engages fewer hot spots on uPAR (Figure 3b). Only one of the uPAR hot-spot residues (Leu-66) comes in contact with **3** (IPR-737). Interestingly, analysis of the crystal structure of uPAR in complex with the

DOI: 10.1021/acs.biochem.6b01039
Biochemistry XXXX, XXX, XXX−XXX

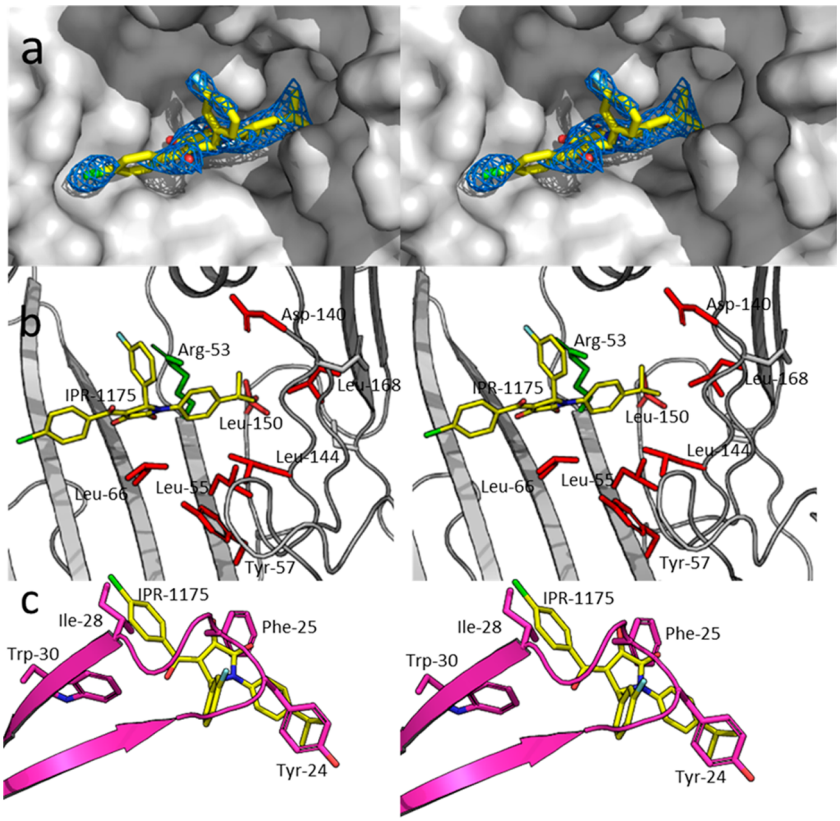

Figure 2. Mode of binding of **12** (IPR-1175) upon the central ligand binding cavity of suPARcc. suPARcc is shown as a gray solvent-accessible surface. **12** (IPR-1175) is shown as capped sticks. Atoms are color-coded by atom type with N, C, O, Cl, and F colored blue, yellow, red, green, and light blue, respectively. The $2F_o - F_c$ electron density map of **12** (IPR-1175) at 1σ is colored blue. (b) Crystal structure of **12** (IPR-1175) bound to uPAR except that uPAR is shown as capped sticks to highly hot-spot residues located within the uPAR cavity. Hot spots are shown as red capped sticks. Arg-53, which is not considered a hot spot, is colored green. (c) Crystal structure of the uPAR·**12** (IPR-1175) complex superimposed on the structure of the uPAR·uPA_{ATF} complex to illustrate the overlap between hot spots on uPA and substituents on **12** (IPR-1175).

AE-147 peptide shows that two hydrophobic residues on the peptide (Phe-5 and Tyr-8) come in direct contact with Ile-66 of uPAR (Figure 1b). Hence, interaction with Ile-66 may explain why **3** (IPR-737) can disrupt binding of AE-147 to uPAR. Engagement of Ile-66, however, is not sufficient to disrupt the full uPAR·uPA_{ATF} interaction. Ile-66 of **3** (IPR-737) binds to uPAR at a site that is occupied by Ile-28 and Trp-30 of uPA. These two residues are located on the β strands of the β hairpin of the GFD domain of uPA (Figure 3c). This is in contrast to **12** (IPR-1175), which overlaps with amino acids located on the loop region of the β hairpin (Figure 2c).

Structure–Activity Relationship. We prepared 46 derivatives of **1** (IPR-1110) to explore the uPAR binding site at the uPAR·uPA interface. Substituents at R_1–R_3 of **1** (IPR-1110) were explored. The binding mode of **12** (IPR-1175) (Figure 2a,b) shows that R_1 groups point toward a large hydrophobic cavity occupied by several uPA hot-spot residues. An aromatic group at R_1 was generally required for inhibition of uPAR·uPA interaction. This is evidenced by complete loss of activity of **25** (IPR-1177), which lacks an aromatic ring at R_1. There are six compounds without an aromatic ring directly attached to the central pyrrolidone ring: **26**, **32**, **34**, **38**, **39**, and **46**; in these compounds, a methylene (**34**) or an ethylene (**26**, **32**, **38**, **39**, and **46**) group separates the central pyrrolinone ring with a benzene ring. Except for **26**, **34**, and **38**, the compounds retained the ability to inhibit the uPAR·uPA protein–protein interaction with IC_{50} values similar to that of **1** (IPR-1110) for **39** and **46**. All three compounds that did not inhibit uPAR·uPA interaction have fluorine atoms on the aromatic ring at R_1, suggesting that highly polar groups may not be suitable for the binding site on uPAR. Interestingly, the compounds bind to uPAR with a K_i of 1–2 μM. Replacing the bromine atom at R_1 with an iodine such as in **13** (IPR-1171) had no effect on the IC_{50} but gave a 2-fold reduction in binding affinity. Removal of the bromine group at the *meta* position and replacing the methyl group with an isopropoxy group in **12** (IPR-1175) or a *tert*-butyl group such as in **15** (IPR-1195) led to a 2–3-fold increase in the IC_{50} and a nearly 2-fold increase in K_i. A benzyloxy group in **16** (IPR-1186) increased the IC_{50} and K_i by 3-fold versus those of **1** (IPR-1110). Generally, replacing the hydrogen atoms at the *meta* position of the aromatic ring directly attached to the central pyrrolidone ring reduced activity substantially as evidenced by a 5-fold increase in IC_{50} and a 20-fold increase in K_i for **37**. Larger groups at one of the *meta* positions were also generally undesirable as most compounds had pronounced increases in IC_{50} such as **36** and **41**. For these compounds, it is interesting that **36** retained almost all of its binding affinity as evidenced by a K_i of 1.9 μM that was 2-fold higher than that of **1** (IPR-1110). Compound **41** had reduced affinity, but its K_i value was within 10 μM. Introduction of various substituents at the *para* position generally weakened the ability to disrupt the uPAR·uPA protein–protein interaction (e.g., **19** and **36**), except for **44** (IPR-1607) and **45** (IPR-2260). Both of these compounds had IC_{50} values similar to that of **1** (IPR-1110). Interestingly, the compound showed a nearly 2-

DOI: 10.1021/acs.biochem.6b01039
Biochemistry XXXX, XXX, XXX–XXX

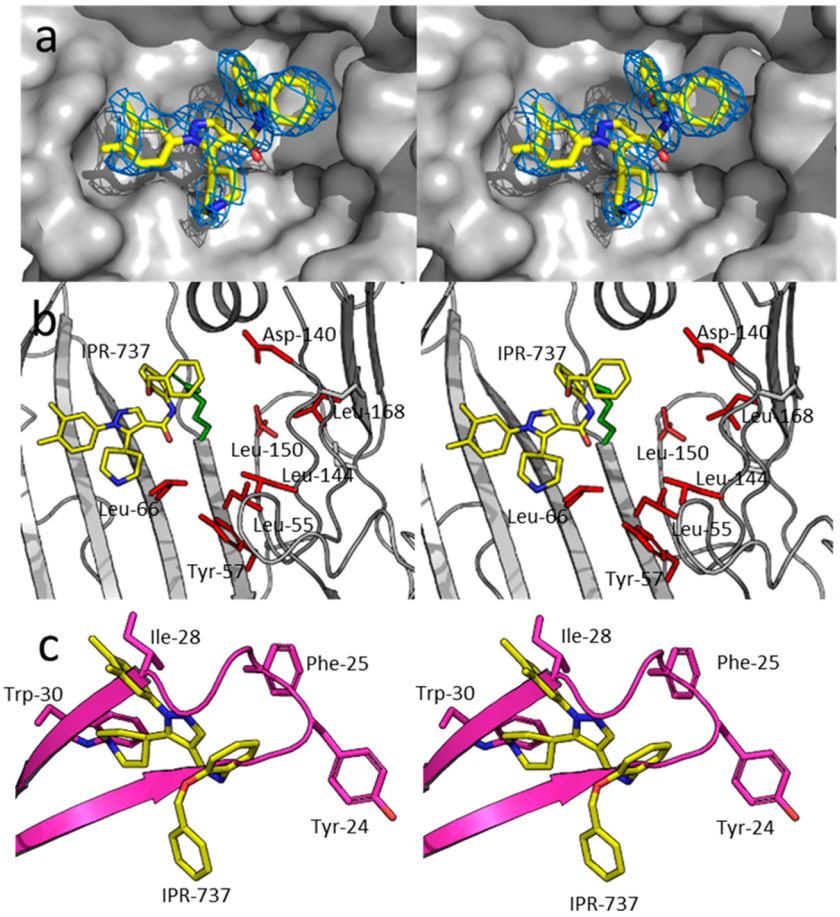

Figure 3. Mode of binding of **3** (IPR-737) upon the central ligand binding cavity of suPARcc. suPARcc is shown as a gray solvent-accessible surface. **3** (IPR-737) is shown as capped sticks. Atoms are color-coded by atom type with N, C, O, Cl, and F colored blue, yellow, red, green, and light blue, respectively. A $2F_o - F_c$ electron density map of **3** (IPR-737) at 1σ is colored blue. (b) Crystal structure of **3** (IPR-737) bound to uPAR except that uPAR is shown as capped sticks to highly hot-spot residues located within the uPAR cavity. Hot spots are shown as red capped sticks. (c) Crystal structure of the uPAR·**3** (IPR-737) complex superimposed on the structure of the uPAR·uPA_{ATF} complex to illustrate the overlap between hot spots on uPA and substituents on **3** (IPR-737).

fold increase in its binding affinity for uPAR as evidenced by a K_i of 0.4 μM compared with a K_i of 0.9 μM for **1** (IPR-1110).

Despite the highly favorable cation−π interaction of the R_2 group with Arg-53, the substituent has significant exposure to solvent. The addition of a methoxy group at the *meta* position of the aromatic ring of R_2 (**21** and **28**) reduced the binding affinity and weakened the potency for inhibition of uPAR·uPA interaction. Replacing the fluorine on **4** (IPR-1201) with a chlorine on **7** (IPR-1178), however, does not have much impact on the binding affinity or inhibition of uPAR·uPA. Moving the fluorine from the *meta* to *ortho* position on **10** reduces the K_i and IC_{50} by 2-fold. It is interesting to note that a methoxy group at the *meta* position of **21** has a much more significant impact on both binding with a 10-fold reduction in K_i and inhibition of the protein−protein interaction as evidenced by a nearly 5-fold increase in IC_{50}. Replacing the hydrogen atom with a fluorine atom of this compound to generate **28** improves the K_i and IC_{50} by 5-fold versus those of compound **21**. In compound **24**, we introduced a *tert*-butyl group at the *para* position of the aromatic ring at R_2, which led to complete abrogation of the inhibition of uPAR·uPA interaction (IC_{50} not determined), although direct binding to uPAR was still detected but its level was reduced by more than an order of magnitude (K_i = 15.9 ± 2.8 μM). A nearly similar effect was observed for **33** (IPR-1157), and an even more dramatic effect when a methoxy group was introduced at the *para* position of R_2 with no inhibition or binding detected within the 100 μM range.

Molecular Dynamics Simulations and Free Energy Calculations. To further explore the interaction between compounds and individual amino acids at the uPAR·uPA interface, we resorted to explicit-solvent molecular dynamics simulations and free energy calculations. We also performed free energy decomposition calculations to investigate the interaction of each amino acid with the compounds. First, we generated a model for the structure of 12 derivatives of **1** (IPR-1110) bound to uPAR using the binding mode of **12** (IPR-1175). These compounds were selected to ensure a uniform distribution across the range of binding affinities. Along with **3** (IPR-737) and **12** (IPR-1175), these complexes were subjected to 100 ns explicit-solvent molecular dynamics simulations. Snapshots were collected at regular intervals, and free energy calculations using the MM-GBSA approach were conducted for each of the compounds as shown in Figure 4a and Table S4. It is worth noting that end-point free energy calculations cannot accurately reproduce the absolute value of the free energy of binding. These calculations, however, have been shown in numerous studies, including ours, to accurately rank-order protein−compound complexes. The MM-GBSA free energy consists of five components, namely, the nonpolar and polar

DOI: 10.1021/acs.biochem.6b01039
Biochemistry XXXX, XXX, XXX−XXX

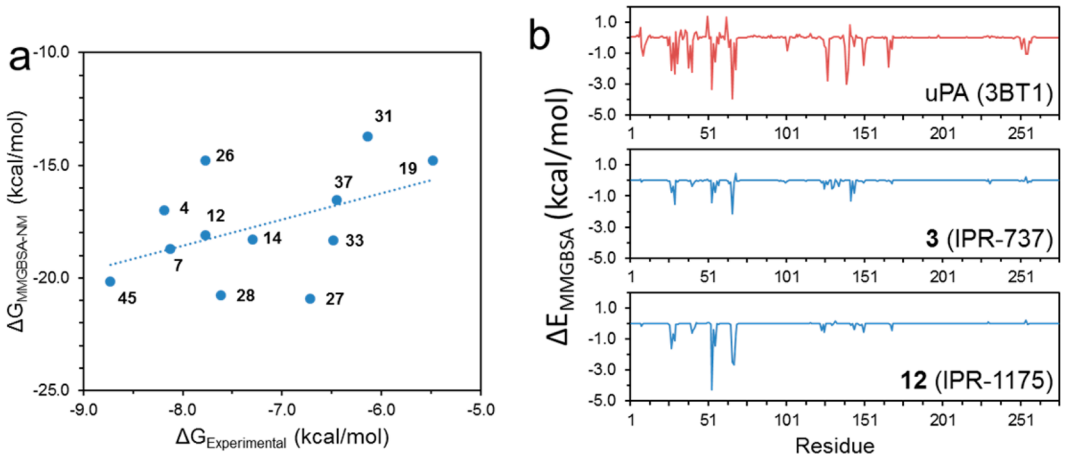

c

Compound	ΔE_{R25}	ΔE_{T27}	ΔE_{L40}	ΔE_{K50}	ΔE_{T51}	ΔE_{R53}	ΔE_{L55}	ΔE_{Y57}	ΔE_{L66}	ΔE_{D102}	ΔE_{S104}	ΔE_{E106}	ΔE_{V125}	ΔE_{E127}	ΔE_{D140}	ΔE_{D141}	ΔE_{H143}	ΔE_{L144}	ΔE_{L150}	ΔE_{P151}	ΔE_{L168}
uPA (3BT1)	-0.54	-2.14	-2.25	1.40	-0.06	-3.33	-1.60	-0.43	-3.93	-0.22	0.02	-0.01	-0.53	-2.79	-2.09	0.80	-0.01	-0.58	-1.77	-0.48	-0.76
3 (IPR-737)	-0.05	-0.78	-0.38	0.09	0.00	-1.41	-0.74	-0.32	-2.12	0.05	0.00	0.03	-0.52	-0.23	0.05	0.04	-0.01	-0.82	-0.12	0.00	-0.22
31 (IPR-1151)	-0.02	-0.87	-0.23	0.13	0.01	-3.75	-1.74	-0.07	-2.37	0.02	0.00	0.02	-0.55	-0.10	0.03	0.03	-0.01	-0.56	-0.53	-0.01	-0.23
19 (IPR-1152)	0.02	-1.47	-0.46	0.08	0.03	-3.53	-1.38	-0.07	-2.28	0.02	0.00	0.02	-0.69	-0.08	0.02	0.03	-0.02	-0.42	-0.63	-0.01	-0.46
33 (IPR-1157)	-0.07	-0.84	-0.08	0.10	0.02	-3.98	-1.90	-0.09	-2.28	0.02	0.00	0.02	-0.90	-0.21	0.03	0.03	-0.03	-0.67	-0.67	-0.01	-0.56
37 (IPR-1161)	0.01	-1.87	-0.60	0.14	0.03	-3.46	-1.46	-0.06	-2.64	0.02	0.00	0.01	-0.63	-0.10	0.03	0.03	-0.02	-0.55	-0.47	-0.01	-0.23
12 (IPR-1175)	0.01	-1.60	-0.58	0.08	0.04	-4.24	-1.41	-0.07	-2.50	0.02	0.00	0.01	-0.55	0.00	0.03	0.02	-0.01	-0.39	-0.53	-0.01	-0.40
7 (IPR-1178)	-0.07	-0.80	-0.13	0.07	0.02	-3.87	-2.13	-0.11	-2.32	0.02	0.00	0.02	-0.93	-0.18	0.02	0.03	-0.02	-0.65	-0.62	-0.01	-0.50
26 (IPR-1188)	-0.03	-0.93	-0.20	0.14	0.01	-3.83	-1.72	-0.16	-2.30	0.01	0.00	0.02	-0.55	-0.12	0.03	0.03	-0.01	-0.47	-0.72	-0.01	-0.29
27 (IPR-1189)	-0.04	-0.70	-0.18	0.07	0.02	-4.58	-1.98	-0.05	-1.90	0.02	0.00	0.02	-0.88	-0.22	0.03	0.03	-0.03	-0.55	-0.69	-0.02	-0.36
28 (IPR-1190)	-0.04	-0.69	-0.15	0.10	-0.01	-3.98	-1.84	-0.09	-2.16	0.02	0.00	0.02	-1.47	-0.50	0.04	0.04	-0.15	-1.01	-0.69	-0.02	-0.57
14 (IPR-1194)	-0.08	-0.77	-0.14	0.13	0.01	-4.86	-1.86	-0.02	-2.36	0.01	0.00	0.01	-0.80	-0.16	0.03	0.03	-0.01	-0.49	-0.67	-0.01	-0.37
4 (IPR-1201)	-0.10	-1.01	-0.31	0.11	-0.01	-3.81	-1.44	-0.19	-2.27	0.03	0.00	0.02	-0.85	-0.19	0.03	0.03	-0.03	-0.73	-0.71	-0.01	-0.43
45 (IPR-2260)	-0.08	-0.96	-0.23	0.14	-0.01	-2.62	-1.24	-0.08	-1.91	0.02	0.00	0.02	-1.16	-0.41	0.04	0.03	-0.03	-0.46	-1.12	-0.17	-1.72

Figure 4. (a) Plot of the MM-GBSA free energy vs inhibition constant K_i that was measured using the fluorescence polarization assay. The correlation coefficients of all 12 selected derivatives are as follows: $r = 0.48$, $\rho = 0.41$, and $\tau = 0.29$. (b) Decomposition of the free energy of binding for uPA, **12** (IPR-1175), and **3** (IPR-737). The decomposition energy consists of the interaction energy between the ligand and each residue on uPAR determined for a collection of snapshots that were obtained from molecular dynamics simulations. (c) Decomposition energies for a select number of hot-spot and non-hot-spot residues for a set of **1** (IPR-1110) derivatives.

potential energies, the polar and nonpolar solvation energies, and the entropy (Table S4). The calculated MM-GBSA free energy correlated positively with the experimentally determined K_i values with a Pearson's r of 0.8, a Spearman's ρ of 0.41, and a Kendall's τ of 0.29 (Figure 4a).

To gain deeper insight into the interaction of the small molecules with individual residues on uPAR, a decomposition energy calculation was performed for each compound (Figure 4b). The decomposition energy consists of polar and nonpolar interaction potential energy, and the polar and nonpolar solvation energies. These calculations were also performed for the uPAR·uPA complex. On uPAR, mutations at 21 residues at the uPAR·uPA interface significantly impaired the interaction.[18] Among these residues, only a subset is considered hot spots by the traditional definition ($\Delta\Delta G > 1$ kcal mol^{-1}). Additionally, not all hot spots are included in this list of residues. We examine the local interaction between uPA and compounds with uPAR at these residues (Figure 4c). As expected, uPA strongly engaged these residues. The change in free energy from the experimental alanine scan correlated with the per-residue decomposition ($r = 0.38$, $\rho = 0.17$, and $\tau = 0.01$). When only hot-spot residues are considered, the correlation decreases to $r = 0.18$, $\rho = 0.11$, and $\tau = 0.10$. At the 21 residues mentioned above, the correlation is $r = 0.11$, $\rho = 0.28$, and $\tau = 0.19$. Comparison of the decomposition energies of **3** (IPR-737) and **12** (IPR-1175) provides insight into the residues that contribute to the ability of **12** to disrupt the protein−protein interaction. Compound **3** (IPR-737) decomposition interaction energies were much weaker than those observed for uPA. In contrast, **12** (IPR-1175) showed much more favorable interaction energies that were comparable to those of uPA, particularly to Thr-27, Leu-55, Leu-66, and Arg-53. It is interesting to note that among all the 21 residues considered, the experimental binding affinity of compounds correlated most strongly with their interaction energies with Leu-150 and Leu-168 with Pearson correlation coefficients of 0.57 and 0.52, respectively (Table S5). In addition, the experimental kinetic rate constants were also compared to the residue decomposition energies of these derivatives (Table S6).

Arg-53 Enhances Binding through Cooperativity. Arg-53 is not considered a hot spot, because alanine scanning studies revealed that it contributes only 0.7 kcal mol^{-1},[18] but it appears to play a critical role in the binding of small molecules as we have demonstrated previously for **2**. Considering the cation−π interaction of **12** with Arg-53, we hypothesized that the residue also plays an essential role in the activity of the compound. We explored the possibility that Arg-53 may be enhancing interaction of the compound with hot spots through cooperative binding. MM-GBSA free energy calculations for double mutants that include Arg-53 were also conducted along with separate MM-GBSA calculations for the individual residues. We ran explicit-solvent molecular dynamics simu-

DOI: 10.1021/acs.biochem.6b01039
Biochemistry XXXX, XXX, XXX−XXX

lations and free energy calculations for both the single- and double-mutation states of the uPAR·uPA (Figure 5a) and uPAR·**12** (Figure 5b) complexes (Table S7).

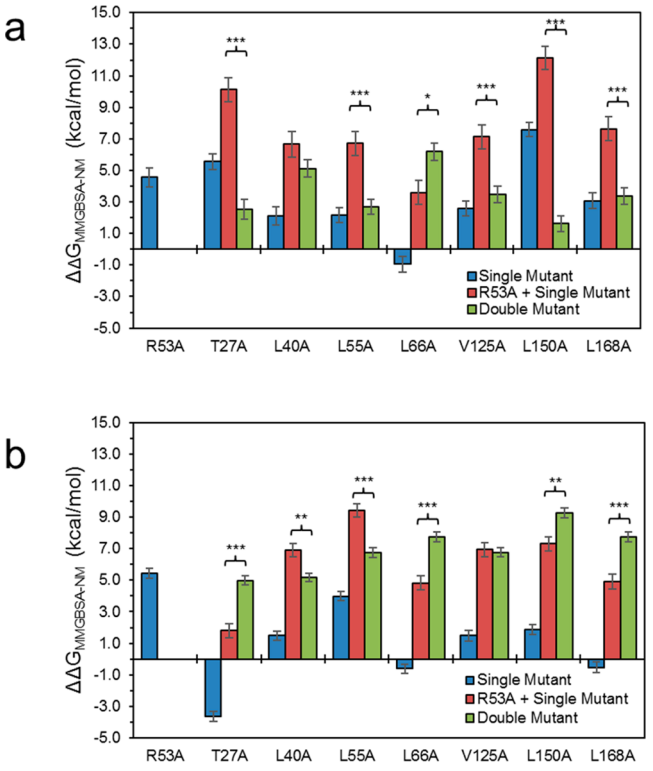

Figure 5. Cooperativity of singly and doubly mutated (a) uPAR·uPA and (b) uPAR·**12** complexes. The difference and standard error between the free energy of each mutant with the respective wild-type complex (blue), the sum of the $\Delta\Delta G$ of the Arg-53-Ala mutant and the single mutant (red), and the double mutant (green). Statistical significance (independent two-sample *t* test): $*p < 0.01$, $**p < 0.001$, and $***p < 0.0001$.

For the uPAR·uPA complex, mutation of all residues except for one (Leu-66) resulted in a penalty in the MM-GBSA free energy consistent with experimental alanine scanning data for these residues (Figure 5a). The sum of the MM-GBSA free energy change as a result of mutation of Arg-53 and each of the amino acids was nearly always unfavorable as shown in Figure 5a. However, it is interesting that when both amino acids (Arg-53 and one of the amino acids in Figure 5) were simultaneously mutated, the resulting change in the MM-GBSA free energy was nearly always different than the sum of the individual mutations (Figure 5a). For example, the sum of the individual mutations of Leu-150 and Arg-53 was 12 kcal mol^{-1}, yet the Leu-150-Ala/Arg-153-Ala double mutation resulted in an only 2 kcal mol^{-1} change in the free energy of binding. Another interesting example is that of Leu-66, for which the sum of individual mutations of this residue and Arg-153 to alanine was 4 kcal mol^{-1}, yet the double mutant was much less favorable at nearly 7 kcal mol^{-1}. These results strongly suggest cooperativity between Arg-53 and hot-spot residues toward the binding of uPA to uPAR. For the uPAR·uPA complex, it appears that Arg-53 significantly reduces the size of the contributions of hot spots to the binding of uPA to uPAR.

We explored whether Arg-53 and other residues bind to **12** in a cooperative manner. In the uPAR·**12** complex, mutation of Thr-27, Leu-66, and Leu-168 resulted in more favorable binding, while mutation of the other residues resulted in a loss of affinity of **12** for uPAR (Figure 5b). Mutation of Arg-53 to alanine, as expected, resulted in the most pronounced effect on the binding of **12** to uPAR. The sum of the contributions of Arg-53 and other residues was unfavorable in nearly every case. Interestingly, double mutants also consistently exhibited an unfavorable effect that was different from the effect of the sum of each mutation. For example, in the case of Thr-27, mutation of this residue along with Arg-53 resulted in a 5 kcal mol^{-1} increase in the free energy of binding compared with only 2 kcal mol^{-1} for the sum of the free energy change of individual mutations. A similar increase was found for Leu-66 and Leu-168. For the other residues, the double mutant showed a change in the free energy less pronounced than the sum of the free energy change for the individual mutations. For example, mutation of Leu-55 and Arg-53 to alanine resulted in a combined free energy change of 9 kcal mol^{-1}, while the Leu-55-Ala/Arg-53-Ala double mutation resulted in a 7 kcal mol^{-1} less favorable interaction. Other than for Val-125, Arg-53 exhibited cooperativity with each of the residues that were considered. Interestingly, double mutants with Arg-53 and another residue all resulted in unfavorable energy for both uPAR·uPA and uPAR·**12** complexes. Interestingly, for two of the hot spots, Leu-66 and Leu-150, Arg-53 enhances the interaction of **12** with uPAR by a combined 5 kcal mol^{-1}, while Arg-53 weakens the interaction of **12** with hot-spot Leu-55 by 2 kcal mol^{-1}.

Small-Molecule uPAR·uPA Inhibitors Alter uPAR Dynamics. The cooperativity among residues prompted us to explore the effect of the two classes of compounds on the dynamics of uPAR. We investigated the correlation of the motion of **3**, **12**, and several other compounds to each residue on uPAR (Figure 6a). Visual inspection of the color-coded map in Figure 6a reveals a dramatic difference in the correlation profile of compounds. For example, pyrrolinone **12** and derivatives generally shows strong correlated motion with residues 1−60 on uPAR, while pyrazole **3** shows no correlation. To compare the effect of **3** and **12** on the dynamics of uPAR with uPA, we generated a cross-correlated map of the motion of uPAR in the presence of uPA (Figure 6b). Interestingly, the effects of **12** on the dynamics of uPAR were remarkably similar to those of uPA on uPAR (Figure 6c,e), while **3** (Figure 6d) showed little correlation. These results suggest small molecules that replicate the dynamics of the native ligand in a protein−protein interaction are more likely to disrupt the interaction.

DISCUSSION

Protein−protein interactions range from transient to tight. Transient interactions are weaker micromolar-affinity interactions that typically involve simpler binding epitopes such as a linear peptide bound to a cavity.[61,62] Tight interactions occur between proteins with single- or double-digit nanomolar-range binding constants. Tight interactions involve larger interfaces (1000−3000 Å^2) with binding epitopes consisting of a single secondary structure such as an α helix, or a more complex binding epitope that spans multiple secondary structures.[1,2,63] While there are numerous examples of small molecules that disrupt weak protein−protein interactions, only a few tight interactions have been successfully inhibited with small molecules.[1] Despite the smaller footprint of small molecules compared with the large protein−protein interface of tight interactions with complex epitopes, it has been suggested that small molecules disrupt these interactions by engaging hot

DOI: 10.1021/acs.biochem.6b01039
Biochemistry XXXX, XXX, XXX−XXX

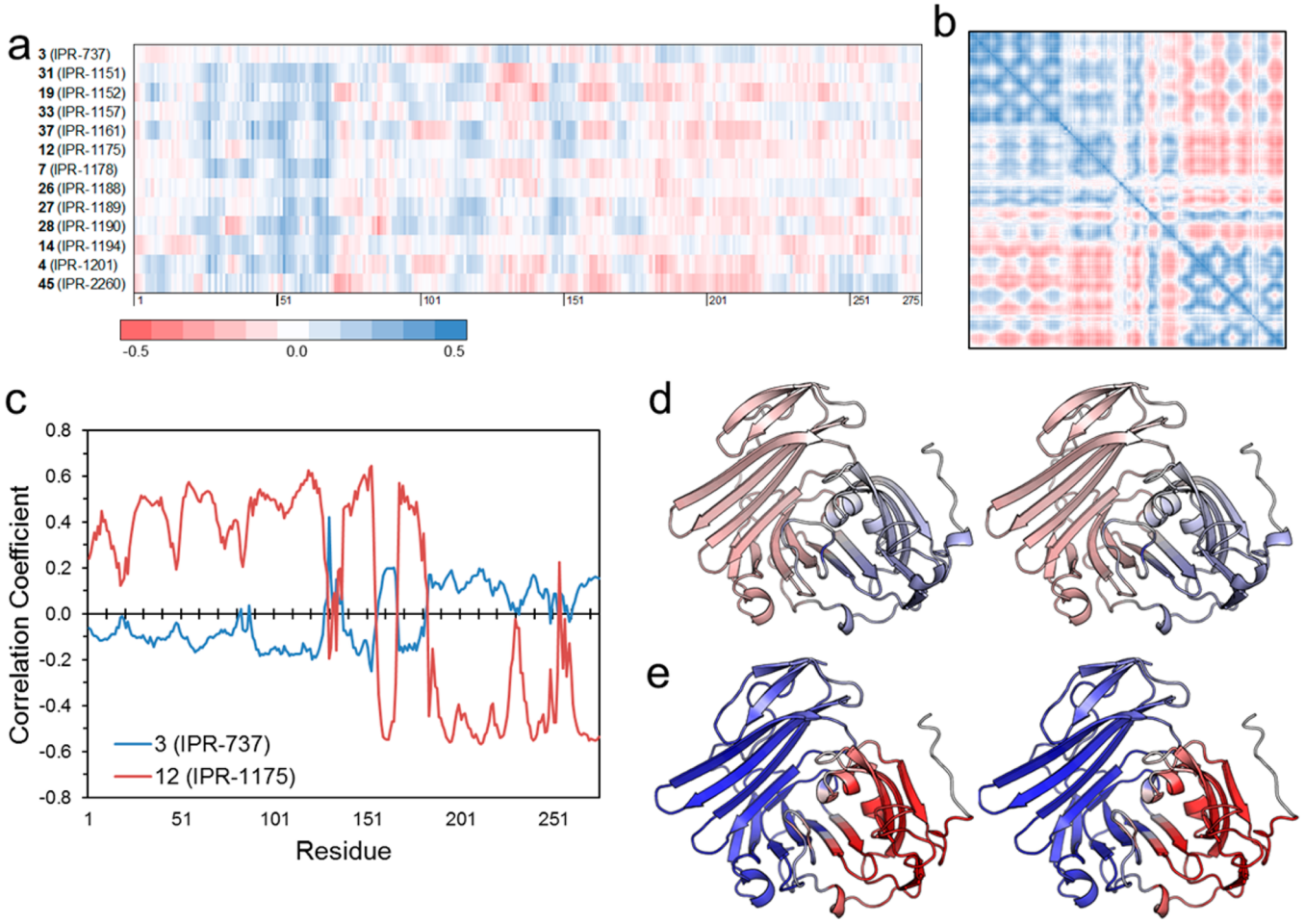

Figure 6. (a) Dynamic cross-correlation matrix (DCCM) cross section of **3** and select derivatives of **1** with uPAR. (b) DCCM of uPAR in the uPAR·uPA complex, colored using the same scheme used for panel a. (c) Pearson's correlation between the cross-correlation of uPAR·**3** and uPAR·**12** complexes and the cross-correlation of individual residues of uPAR in the uPAR·uPA complex. Stereoviews of three-dimensional structures of uPAR in the (d) uPAR·**3** and (e) uPAR·**12** complexes, colored on the basis of the correlation coefficient in panel c from positive correlation (blue) to no correlation (white) to negative correlation (red).

spots at the interface.[9,26,27] Hot spots can be located on either the ligand or the receptor binding cleft.[5,8,64]

Here, we explore small-molecule antagonists of the uPAR·uPA interaction, a tight and stable protein−protein interaction. The uPAR·uPA interface has a well-defined binding cavity that contains multiple hot-spot residues that contribute ≥1 kcal mol^{-1} to the binding affinity. These hot spots are located on both uPAR and its ligand, uPA. Small molecules that (i) mimic the position of hot spots on the ligand (uPA) and (ii) engage hot spots on the receptor (uPAR) are expected to disrupt this interaction. Previously, we had identified two classes of compounds that disrupt the protein−protein interaction. The first compound, **2**, was identified by docking a commercial library to an ensemble of structures of uPAR collected from molecular dynamics simulations.[24] The compound showed binding affinity in the submicromolar range and an IC_{50} for disruption of uPAR·uPA interaction in the single-digit micromolar range. Interestingly, the predicted mode of binding of **2** to a structure of uPAR sampled from molecular dynamics simulation revealed a salt bridge between the benzoic acid moiety of **2** and Arg-53.[24] A recent crystal structure of an analogue of **2** bound to uPAR confirmed our predicted binding mode of the compound and supported the existence of a salt-bridge interaction with Arg-53.[20] Arg-53 is buried in the crystal structure of the uPAR·uPA complex. The snapshot of **2** bound to uPAR that emerged from our molecular dynamics simulations revealed an exposed Arg-53. Interestingly, the apo structure of uPAR, which was determined after we discovered **2**, reveals an exposed Arg-53.[65] This supported our rationale for using molecular dynamics simulations to sample conformations that differ from the structure of uPAR in its complex with uPA. The second class of uPAR·uPA antagonists that we discovered were pyrrolinone compounds.[23] Interestingly, these compounds were identified in a ligand-based approach using the structure of pyrazole, pyrrolodinone, piperidinone, and butanamine compounds that were identified by structure-based virtual screening using the structure of uPAR from the uPAR·uPA complex.[21] The carbon that bears the hydroxyl group of the pyrrolinone compounds considered in this work may be prone to attack by nucleophiles. However, the OH group makes a poor leaving group, making covalent adduct formation between the compound and protein unlikely. We confirmed this with mass spectrometry. Further evidence that argues against the formation of a covalent adduct is the fact that replacement of OH with a methoxy or isopropoxy, each of which is a much better leaving group than OH is, resulted in lower-affinity compounds. Also, the lack of exposed nucleophiles such as cysteine residues on uPAR makes it highly

DOI: 10.1021/acs.biochem.6b01039
Biochemistry XXXX, XXX, XXX−XXX

unlikely that **1** and derivatives covalently attach to uPAR. In addition, we show that the compound is stable in buffer, methanol, and uPAR.

We synthesize nearly 50 derivatives of pyrollinone **1** to explore the uPAR·uPA protein−protein interaction. We determined the crystal structure of a derivative of **1**, namely **12** (IPR-1175), and a pyrazole compound **3** (IPR-737) that binds to uPAR but does not disrupt the uPAR·uPA interface. The structures reveal that the pyrazole compounds bind to a site on uPAR that is occupied by a uPA side chain located on the β strands of the β turn of the GFD domain of uPA. The 2-pyrrolinone compound, however, adopts a different binding mode. In addition, the compound comes in direct contact with several hot spots. This explains why both compounds bind to uPAR but only the 2-pyrrolone inhibits uPAR·uPA interaction within the 100 μM concentration range considered in this work. It was interesting that two of the aromatic rings of **12** engaged Arg-53, directly forming highly favorable cation−π interactions. Cation−π interactions are electrostatic interactions that are considered to be among the strongest noncovalent interactions in protein structures,[66] while mutation of this residue seems to be a common feature of small molecules that we have found to inhibit the uPAR·uPA protein−protein interaction. Previously, we found that a salt-bridge interaction between a benzoic acid moiety on **2** (IPR-803) and the guanidinium ion of Arg-53 was the critical factor that led to inhibition of uPAR·uPA interaction.[24] Removal of the benzoic acid led to loss of inhibition of the protein−protein interaction. The use of hot spots on uPAR and uPA in future studies is expected to lead to derivatives that are substantially more potent than the parent compound. This could be achieved by enhancing the affinity of compounds to individual hot-spot residues or by mimicking critical hot spots located on uPA, such as Phe-25 or Trp-30.

While Arg-53 is not considered a hot spot, its interaction with small molecules appears to be essential for successful inhibition of the uPAR·uPA interaction by small molecules. Interestingly, molecular dynamics simulation-based free energy decomposition reveals that Arg-53 makes the strongest interaction with uPA compared with other uPA residues that come in contact with uPAR. Despite the strong interaction, alanine scanning studies show that Arg-53 only moderately contributes to the binding affinity (0.7 kcal mol^{-1}[11]). This can be explained by the fact that decomposition energies do not take into consideration the configurational entropy contributions to the binding, in contrast to the alanine scanning that used surface plasmon resonance, which includes both enthalpy and entropy. Considering the position of Arg-53 within the core structure of uPAR, it is possible that mutation of Arg-53 may have destabilized uPAR and hence enhanced entropy contributions to the binding affinity, despite the significant loss of enthalpy. Small-molecule inhibitors are expected to disrupt only the interaction of residues and not their contributions to the entropy of binding. This suggests that residues that are not considered hot spots should not be ignored in the design of small-molecule protein−protein interaction inhibitors.

The discovery of hot spots at protein−protein interfaces was a significant breakthrough in the field of protein−protein interaction drug discovery. The primary tools to identify hot spots is to systematically mutate each residue to alanine and measure the effect on the binding thermodynamics and kinetics. This process is known as alanine scanning. One limitation of these alanine scanning experiments is that they do not consider the effects of neighboring residues, which may enhance or weaken the contributions of individual residues.[67,68] How to take advantage of hot spots for small-molecule drug discovery is still unclear. To gain deeper insight into the role of Arg-53 in the binding of the small-molecule inhibitors, we explored whether any cooperativity between the residue and other residues that come in contact with **1** exists. Interestingly, we found that the independent mutation of Arg-53 and other hot spots resulted in changes in the predicted binding affinity that were different from those measured when both Arg-53 and hot spots were mutated. For uPA, mutation of hot spots resulted in a less favorable MM-GBSA free energy for six of the seven mutations, yet mutations of Arg-53 and each of these residues resulted in dramatically different free energy changes. For example, the mutation of Arg-53 and Leu-150 led to a combined 13 kcal mol^{-1} MM-GBSA free energy change, yet the combined mutation of these two residues resulted in a change of only 2 kcal mol^{-1}, a dramatic difference. For compound **12**, mutation of Arg-53 and Leu-150 led to MM-GBSA free energy changes of 6 and 2 kcal mol^{-1}, respectively. This is in contrast to the dual mutation of both residues that resulted in an unfavorable change of >9 kcal mol^{-1}.

In summary, our work provides insight into the forces that drive small molecules to disrupt tight and stable protein−protein interactions. We show that mere binding is not a sufficient requirement for disrupting the uPAR·uPA protein−protein interaction. Even binding to hot-spot residues is not a guarantee of disruption of the protein−protein interaction. We find that residues that are not considered hot spots in alanine scanning experiments such as Arg-53 in uPAR can provide a strong anchor for small molecules to enhance their binding affinity. These anchors can also strengthen binding of small molecules to other hot spots through cooperativity. Also, salt-bridge and π−cation interactions appear to be critical for disruption of the uPAR·uPA interaction. A previously discovered uPAR antagonist, IPR-803, formed a salt-bridge interaction that was essential for inhibition of uPAR·uPA interaction,[24] and compounds reported in this work bind to Arg-53 through π−cation interactions. These types of interactions are likely to be favorable at protein−protein interfaces considering the shallow nature of the pockets and the high degree of solvent exposure. These interactions may be a straightforward strategy for enhancing the inhibition potency of compounds that bind to the target. Another important finding of this work is the importance of molecular dynamics in the inhibition of tight PPIs by small molecules. We discovered that small molecules that inhibit uPAR·uPA interaction alter the dynamics of uPAR in a manner similar to that of uPA. This suggests that drug discovery efforts targeting protein−protein interactions should also consider the effect of compounds on the dynamics of the receptor as opposed to merely focusing on the interaction energy. Small molecules that bind tightly to hot spots and also modulate the dynamics of the receptor in a manner similar to that of the native tight ligand are expected to lead to more effective inhibitors. These findings can help guide the design of derivatives of IPR-1110 through modification of the core structure of the compound or by the introduction of new substituents.

DOI: 10.1021/acs.biochem.6b01039
Biochemistry XXXX, XXX, XXX−XXX

■ ASSOCIATED CONTENT

Supporting Information

The Supporting Information is available free of charge on the ACS Publications website at DOI: 10.1021/acs.biochem.6b01039.

Chemical structures of compounds that emerged from virtual screening against the uPAR crystal structure and multiple conformers, hot spots on uPAR of the uPAR·uPA interaction, adapted from ref 18 (Table S1), X-ray data collection and refinement statistics of the suPARcc·**12** (IPR-1175) complex (Table S2), X-ray data collection and refinement statistics of the suPARcc·**3** (IPR-737) complex (Table S3), calculated free energies ± the standard error of **3** and select derivatives of **1**, showing the individual free energy terms (Table S4), correlation coefficients of the individual free energy terms and correlation to select residues of uPAR to illustrate the relationship between the decomposition energy and inhibition constant K_i for select derivatives of **1** from Figure 4c (Table S5), correlation coefficients to illustrate the relationship between the decomposition energy of select residues from Figure 4c and kinetic rate constants for select derivatives of **1** (Table S6), and calculated free energies ± the standard error of single and double mutants in the uPAR·uPA and uPAR·**12** complexes (Table S7) (PDF)

■ AUTHOR INFORMATION

Corresponding Author

*Departments of Biochemistry and Molecular Biology, Indiana University School of Medicine, 410 W. 10th St., HITS 5000, Indianapolis, IN 46202. E-mail: smeroueh@iu.edu. Telephone: (317) 274-8315. Fax: (317) 278-9217.

ORCID

Mingdong Huang: 0000-0002-1377-6786

Samy O. Meroueh: 0000-0002-3948-7499

Author Contributions

D.L. and D.X. contributed equally to this work.

Funding

The research was supported by the National Institutes of Health (CA135380) (S.O.M.), American Cancer Society Research Scholar Grant RSG-12-092-01-CDD (S.O.M.), and the 100 Voices of Hope (S.O.M.). Computer time on the Big Red II and Karst supercomputer at Indiana University (S.O.M.) is supported in part by Lilly Endowment, Inc., through its support for the Indiana University Pervasive Technology Institute, and in part by the Indiana METACyt Initiative.

Notes

The authors declare no competing financial interest.

■ REFERENCES

(1) Arkin, M. R., Tang, Y., and Wells, J. A. (2014) Small-Molecule Inhibitors of Protein-Protein Interactions: Progressing Toward the Reality. *Chem. Biol. 21*, 1102−1114.

(2) Watkins, A. M., and Arora, P. S. (2015) Structure-based inhibition of protein-protein interactions. *Eur. J. Med. Chem. 94*, 480−488.

(3) Oltersdorf, T., Elmore, S. W., Shoemaker, A. R., Armstrong, R. C., Augeri, D. J., Belli, B. A., Bruncko, M., Deckwerth, T. L., Dinges, J., Hajduk, P. J., et al. (2005) An inhibitor of Bcl-2 family proteins induces regression of solid tumours. *Nature 435*, 677−681.

(4) Wilson, C. G., and Arkin, M. R. (2013) Probing structural adaptivity at PPI interfaces with small molecules. *Drug Discovery Today: Technol. 10*, e501−508.

(5) Cukuroglu, E., Engin, H. B., Gursoy, A., and Keskin, O. (2014) Hot spots in protein-protein interfaces: towards drug discovery. *Prog. Biophys. Mol. Biol. 116*, 165−173.

(6) Kortemme, T., and Baker, D. (2002) A simple physical model for binding energy hot spots in protein-protein complexes. *Proc. Natl. Acad. Sci. U. S. A. 99*, 14116−14121.

(7) Clackson, T., and Wells, J. A. (1995) A Hot Spot of Binding Energy in a Hormone-Receptor Interface. *Science 267*, 383−386.

(8) Keskin, O., Ma, B., and Nussinov, R. (2005) Hot regions in protein−protein interactions: the organization and contribution of structurally conserved hot spot residues. *J. Mol. Biol. 345*, 1281−1294.

(9) Bogan, A. A., and Thorn, K. S. (1998) Anatomy of Hot Spots in Protein Interfaces. *J. Mol. Biol. 280*, 1−9.

(10) Magdolen, V., Rettenberger, P., Koppitz, M., Goretzkt, L., Kessler, H., Weidle, U. H., Konig, B., Graeff, H., Schmitt, M., and Wilhelm, O. (1996) Systematic Mutational Analysis of the Receptor-Binding Region of the Human Urokinase-Type Plasminogen Activator. *Eur. J. Biochem. 237*, 743−751.

(11) Gardsvoll, H., and Ploug, M. (2007) Mapping of the vitronectin-binding site on the urokinase receptor: involvement of a coherent receptor interface consisting of residues from both domain I and the flanking interdomain linker region. *J. Biol. Chem. 282*, 13561−13572.

(12) Madsen, C. D., Ferraris, G. M., Andolfo, A., Cunningham, O., and Sidenius, N. (2007) uPAR-induced cell adhesion and migration: vitronectin provides the key. *J. Cell Biol. 177*, 927−939.

(13) Huai, Q., Zhou, A., Lin, L., Mazar, A. P., Parry, G. C., Callahan, J., Shaw, D. E., Furie, B., Furie, B. C., and Huang, M. (2008) Crystal structures of two human vitronectin, urokinase and urokinase receptor complexes. *Nat. Struct. Mol. Biol. 15*, 422−423.

(14) Lin, L., Gardsvoll, H., Huai, Q., Huang, M., and Ploug, M. (2010) Structure-based engineering of species selectivity in the interaction between urokinase and its receptor: implication for preclinical cancer therapy. *J. Biol. Chem. 285*, 10982−10992.

(15) Gardsvoll, H., Dano, K., and Ploug, M. (1999) Mapping part of the functional epitope for ligand binding on the receptor for urokinase-type plasminogen activator by site-directed mutagenesis. *J. Biol. Chem. 274*, 37995−38003.

(16) Huai, Q., Mazar, A. P., Kuo, A., Parry, G. C., Shaw, D. E., Callahan, J., Li, Y., Yuan, C., Bian, C., and Chen, L. (2006) Structure of human urokinase plasminogen activator in complex with its receptor. *Science 311*, 656−659.

(17) Llinas, P., Hélène Le Du, M., Gardsvoll, H., Dano, K., Ploug, M., Gilquin, B., Stura, E. A., and Menez, A. (2005) Crystal structure of the human urokinase plasminogen activator receptor bound to an antagonist peptide. *EMBO J. 24*, 1655−1663.

(18) Gardsvoll, H., Gilquin, B., Le Du, M. H., Menez, A., Jorgensen, T. J., and Ploug, M. (2006) Characterization of the functional epitope on the urokinase receptor. Complete alanine scanning mutagenesis supplemented by chemical cross-linking. *J. Biol. Chem. 281*, 19260−19272.

(19) Chen, Z., Lin, L., Huai, Q., and Huang, M. (2009) Challenges for drug discovery-a case study of urokinase receptor inhibition. *Comb. Chem. High Throughput Screening 12*, 961.

(20) Mani, T., Wang, F., Knabe, W. E., Sinn, A. L., Khanna, M., Jo, I., Sandusky, G. E., Sledge, G. W., Jr., Jones, D. R., Khanna, R., Pollok, K. E., and Meroueh, S. O. (2013) Small-molecule inhibition of the uPAR.uPA interaction: synthesis, biochemical, cellular, in vivo pharmacokinetics and efficacy studies in breast cancer metastasis. *Bioorg. Med. Chem. 21*, 2145−2155.

(21) Mani, T., Liu, D., Zhou, D., Li, L., Knabe, W. E., Wang, F., Oh, K., and Meroueh, S. O. (2013) Probing binding and cellular activity of pyrrolidinone and piperidinone small molecules targeting the urokinase receptor. *ChemMedChem 8*, 1963−1977.

(22) Wang, F., Eric Knabe, W., Li, L., Jo, I., Mani, T., Roehm, H., Oh, K., Li, J., Khanna, M., and Meroueh, S. O. (2012) Design, synthesis, biochemical studies, cellular characterization, and structure-based

DOI: 10.1021/acs.biochem.6b01039
Biochemistry XXXX, XXX, XXX−XXX

computational studies of small molecules targeting the urokinase receptor. *Bioorg. Med. Chem. 20*, 4760−4773.
(23) Liu, D., Zhou, D., Wang, B., Knabe, W. E., and Meroueh, S. O. (2015) A New Class of Orthosteric uPAR.uPA Small-Molecule Antagonists Are Allosteric Inhibitors of the uPAR.Vitronectin Interaction. *ACS Chem. Biol. 10*, 1521−1534.
(24) Khanna, M., Wang, F., Jo, I., Knabe, W. E., Wilson, S. M., Li, L., Bum-Erdene, K., Li, J., Sledge, G. W., Khanna, R., and Meroueh, S. O. (2011) Targeting multiple conformations leads to small molecule inhibitors of the uPAR.uPA protein-protein interaction that block cancer cell invasion. *ACS Chem. Biol. 6*, 1232−1243.
(25) Rullo, A. F., Fitzgerald, K. J., Muthusamy, V., Liu, M., Yuan, C., Huang, M., Kim, M., Cho, A. E., and Spiegel, D. A. (2016) Re-engineering the Immune Response to Metastatic Cancer: Antibody-Recruiting Small Molecules Targeting the Urokinase Receptor. *Angew. Chem., Int. Ed. 55*, 3642.
(26) Kortemme, T., and Baker, D. (2002) A simple physical model for binding energy hot spots in protein-protein complexes. *Proc. Natl. Acad. Sci. U. S. A. 99*, 14116−14121.
(27) Clackson, T., and Wells, J. A. (1995) A hot spot of binding energy in a hormone-receptor interface. *Science 267*, 383−386.
(28) Thanos, C. D., DeLano, W. L., and Wells, J. A. (2006) Hot-Spot Mimicry of a Cytokine Receptor by a Small Molecule. *Proc. Natl. Acad. Sci. U. S. A. 103*, 15422−15427.
(29) Hyde, J., Braisted, A. C., Randal, M., and Arkin, M. R. (2003) Discovery and characterization of cooperative ligand binding in the adaptive region of interleukin-2. *Biochemistry 42*, 6475−6483.
(30) Keskin, Z., Gursoy, A., Ma, B., and Nussinov, R. (2008) Principles of protein-protein interactions: What are the preferred ways for proteins to interact? *Chem. Rev. 108*, 1225−1244.
(31) Jacobsen, B., Gårdsvoll, H., Juhl Funch, G., Ostergaard, S., Barkholt, V., and Ploug, M. (2007) One-step affinity purification of recombinant urokinase-type plasminogen activator receptor using a synthetic peptide developed by combinatorial chemistry. *Protein Expression Purif. 52*, 286−296.
(32) Xu, X., Gardsvoll, H., Yuan, C., Lin, L., Ploug, M., and Huang, M. (2012) Crystal structure of the urokinase receptor in a ligand-free form. *J. Mol. Biol. 416*, 629−641.
(33) Otwinowski, Z., and Minor, W. (1997) Processing of X-ray diffraction data collected in oscillation mode. *Methods Enzymol. 276*, 307−326.
(34) Vagin, A., and Teplyakov, A. (1997) MOLREP: an Automated Program for Molecular Replacement. *J. Appl. Crystallogr. 30*, 1022−1025.
(35) Emsley, P., and Cowtan, K. (2004) Coot: model-building tools for molecular graphics. *Acta Crystallogr., Sect. D: Biol. Crystallogr. 60*, 2126−2132.
(36) Jacobson, M. P., Pincus, D. L., Rapp, C. S., Day, T. J., Honig, B., Shaw, D. E., and Friesner, R. A. (2004) A Hierarchical Approach to All-Atom Protein Loop Prediction. *Proteins: Struct., Funct., Genet. 55*, 351−367.
(37) Sali, A., and Blundell, T. L. (1993) Comparative Protein Modelling by Satisfaction of Spatial Restraints. *J. Mol. Biol. 234*, 779−815.
(38) Olsson, M. H. M., Søndergaard, C. R., Rostkowski, M., and Jensen, J. H. (2011) PROPKA3: Consistent Treatment of Internal and Surface Residues in Empirical pKa Predictions. *J. Chem. Theory Comput. 7*, 525−537.
(39) Halgren, T. A., Murphy, R. B., Friesner, R. A., Beard, H. S., Frye, L. L., Pollard, W. T., and Banks, J. L. (2004) Glide: a new approach for rapid, accurate docking and scoring. 2. Enrichment factors in database screening. *J. Med. Chem. 47*, 1750−1759.
(40) Case, D. A., Berryman, J. T., Betz, R. M., Cerutti, D. S., Cheatham, T. E., III, Darden, T. A., Duke, R. E., Giese, T. J., Gohlke, H., Goetz, A. W., Homeyer, N., Izadi, S., Janowski, P., Kaus, J., Kovalenko, A., Lee, T. S., LeGrand, S., Li, P., Luchko, T., Luo, R., Madej, B., Merz, K. M., Monard, G., Needham, P., Nguyen, H., Nguyen, H. T., Omelyan, I., Onufriev, A., Roe, D. R., Roitberg, A., Salomon-Ferrer, R., Simmerling, C. L., Smith, W., Swails, J., Walker, R. C., Wang, J., Wolf, R. M., Wu, X., York, D. M., and Kollman, P. A. (2015) *AMBER 2015*, University of California, San Francisco.
(41) Jakalian, A., Jack, D. B., and Bayly, C. I. (2002) Fast, Efficient Generation of High-quality Atomic Charges. AM1-BCC Model: II. Parameterization and Validation. *J. Comput. Chem. 23*, 1623−1641.
(42) Wang, J., Wolf, R. M., Caldwell, J. W., Kollman, P. A., and Case, D. A. (2004) Development and Testing of a General Amber Force Field. *J. Comput. Chem. 25*, 1157−1174.
(43) Wang, J., Wang, W., Kollman, P. A., and Case, D. A. (2006) Automatic Atom Type and Bond Type Perception in Molecular Mechanical Calculations. *J. Mol. Graphics Modell. 25*, 247−260.
(44) Jorgensen, W. L., Chandrasekhar, J., Madura, J. D., Impey, R. W., and Klein, M. L. (1983) Comparison of Simple Potential Functions for Simulating Liquid Water. *J. Chem. Phys. 79*, 926−935.
(45) Maier, J. A., Martinez, C., Kasavajhala, K., Wickstrom, L., Hauser, K. E., and Simmerling, C. (2015) ff14SB: Improving the Accuracy of Protein Side Chain and Backbone Parameters from ff99SB. *J. Chem. Theory Comput. 11*, 3696−3713.
(46) Ryckaert, J. P., Ciccotti, G., and Berendsen, J. J. C. (1977) Numerical Integration of the Cartesian Equations of Motion of a System with Constraints: Molecular Dynamics of n-Alkanes. *J. Comput. Phys. 23*, 327−341.
(47) Darden, T., York, D., and Pedersen, L. (1993) Particle Mesh Ewald: An N × log(N) Method for Ewald Sums in Large Systems. *J. Chem. Phys. 98*, 10089−10092.
(48) Roe, D. R., and Cheatham, T. E., 3rd (2013) PTRAJ and CPPTRAJ: Software for Processing and Analysis of Molecular Dynamics Trajectory Data. *J. Chem. Theory Comput. 9*, 3084−3095.
(49) Still, W. C., Tempczyk, A., Hawley, R. C., and Hendrickson, T. (1990) Semianalytical Treatment of Solvation for Molecular Mechanics and Dynamics. *J. Am. Chem. Soc. 112*, 6127−6129.
(50) Miller, B. R., 3rd, McGee, T. D., Jr., Swails, J. M., Homeyer, N., Gohlke, H., and Roitberg, A. E. (2012) MMPBSA.py: An Efficient Program for End-State Free Energy Calculations. *J. Chem. Theory Comput. 8*, 3314−3321.
(51) Onufriev, A., Bashford, D., and Case, D. A. (2004) Exploring Protein Native States and Large-scale Conformational Changes with a Modified Generalized Born Model. *Proteins: Struct., Funct., Genet. 55*, 383−394.
(52) Feig, M., Onufriev, A., Lee, M. S., Im, W., Case, D. A., and Brooks, C. L., 3rd (2004) Performance Comparison of Generalized Born and Poisson Methods in the Calculation of Electrostatic Solvation Energies for Protein Structures. *J. Comput. Chem. 25*, 265−284.
(53) Brooks, B., and Karplus, M. (1983) Harmonic Dynamics of Proteins: Normal Modes and Fluctuations in Bovine Pancreatic Trypsin Inhibitor. *Proc. Natl. Acad. Sci. U. S. A. 80*, 6571−6575.
(54) Gohlke, H., Kiel, C., and Case, D. A. (2003) Insights into Protein−Protein Binding by Binding Free Energy Calculation and Free Energy Decomposition for the Ras−Raf and Ras−RalGDS Complexes. *J. Mol. Biol. 330*, 891−913.
(55) Onufriev, A., Bashford, D., and Case, D. A. (2004) Exploring Protein Native States and Large-scale Conformational Changes with a Modified Generalized Born Model. *Proteins: Struct., Funct., Genet. 55*, 383−394.
(56) De Marco, A., De Candia, M., Carotti, A., Cellamare, S., De Candia, E., and Altomare, C. (2004) Lipophilicity-related inhibition of blood platelet aggregation by nipecotic acid anilides. *Eur. J. Pharm. Sci. 22*, 153−164.
(57) Milagre, C. D., Milagre, H. M., Moran, P. J., and Rodrigues, J. A. (2010) Chemoenzymatic synthesis of alpha-hydroxy-beta-methyl-gamma-hydroxy esters: role of the keto-enol equilibrium to control the stereoselective hydrogenation in a key step. *J. Org. Chem. 75*, 1410−1418.
(58) Richter, A., Rose, R., Hedberg, C., Waldmann, H., and Ottmann, C. (2012) An optimized small-molecule stabiliser of the 14−3-3-PMA2 protein-protein interaction. *Chem. - Eur. J. 18*, 6520−6527.

DOI: 10.1021/acs.biochem.6b01039
Biochemistry XXXX, XXX, XXX−XXX

1160 (59) Mahadevi, A. S., and Sastry, G. N. (2013) Cation-pi interaction:
1161 its role and relevance in chemistry, biology, and material science.
1162 *Chem. Rev. 113*, 2100−2138.
1163 (60) Mecozzi, S., West, A. P., and Dougherty, D. A. (1996) Cation-pi
1164 interactions in aromatics of biological and medicinal interest:
1165 electrostatic potential surfaces as a useful qualitative guide. *Proc.*
1166 *Natl. Acad. Sci. U. S. A. 93*, 10566−10571.
1167 (61) Nooren, I. M. A., and Thornton, J. M. (2003) Structural
1168 characterisation and functional significance of transient protein-protein
1169 interactions. *J. Mol. Biol. 325*, 991−1018.
1170 (62) Acuner Ozbabacan, S. E., Engin, H. B., Gursoy, A., and Keskin,
1171 O. (2011) Transient protein−protein interactions. *Protein Eng., Des.*
1172 *Sel. 24*, 635−648.
1173 (63) Pelay-Gimeno, M., Glas, A., Koch, O., and Grossmann, T. N.
1174 (2015) Structure-Based Design of Inhibitors of Protein−Protein
1175 Interactions: Mimicking Peptide Binding Epitopes. *Angew. Chem., Int.*
1176 *Ed. 54*, 8896−8927.
1177 (64) Cukuroglu, E., Gursoy, A., and Keskin, O. (2012) HotRegion: a
1178 database of predicted hot spot clusters. *Nucleic Acids Res. 40*, D829−
1179 833.
1180 (65) Xu, X., Gårdsvoll, H., Yuan, C., Lin, L., Ploug, M., and Huang,
1181 M. (2012) Crystal structure of the urokinase receptor in a ligand-free
1182 form. *J. Mol. Biol. 416*, 629−641.
1183 (66) Dougherty, D. A. (2013) The cation− π interaction. *Acc. Chem.*
1184 *Res. 46*, 885−893.
1185 (67) Vaughan, C. K., Buckle, A. M., and Fersht, A. R. (1999)
1186 Structural response to mutation at a protein-protein interface. *J. Mol.*
1187 *Biol. 286*, 1487−1506.
1188 (68) Schreiber, G., and Fersht, A. R. (1995) Energetics of protein-
1189 protein interactions: analysis of the barnase-barstar interface by single
1190 mutations and double mutant cycles. *J. Mol. Biol. 248*, 478−486.

DOI: 10.1021/acs.biochem.6b01039
Biochemistry XXXX, XXX, XXX−XXX